coatings

MDPI

Article

Thermal Simulation Accuracy for Laser Cladding Fe313/Al via Dilution, Absorptivity & Heat Source Synergy

Bing Zhang, Fangyi You *, Hanyuan Pu, Xian Wu, Yongyi Cai and Hung-Ming Huang

College of Mechanical Engineering and Automation, Huaqiao University, Xiamen 361021, China; zhangbing221016@163.com (B.Z.); 24133080034@stu.hqu.edu.cn (H.P.); xianwu@hqu.edu.cn (X.W.); 25014080004@stu.hqu.edu.cn (Y.C.)

* Correspondence: fangyiy@hqu.edu.cn; Tel.: +86-153-593-76266

Abstract

Aluminum alloys are widely employed in the aerospace industry owing to their lightweight characteristics. Laser cladding offers an effective means to enhance their surface hardness and wear resistance; however, its application is constrained by several inherent challenges: the high thermal conductivity and low laser absorptivity of aluminum substrates, coupled with the property mismatch between the substrate and cladding powder, readily induce stress concentrations and crack formation in the clad layer. High-fidelity temperature field simulation is therefore essential for predicting residual stresses and microstructural evolution. Conventional simulation approaches rely primarily on calibrating heat source parameters to match the molten pool morphology, yet they overlook the dynamic evolution of thermophysical properties arising from compositional variations in the dilution zone—a critical factor that compromises predictive accuracy. To address this limitation, this study proposes a two-step correction strategy that establishes a linkage between composition-dependent thermophysical properties and heat source modeling. In the first step, the target dilution ratio is used to inversely determine the elemental composition within the dilution zone, enabling the recalibration of thermophysical parameters in the melt pool region. This measure reduced temperature simulation deviations near the melt pool from 41% to 17%. In the second step, a sensitivity analysis of the temperature field to heat source parameters reveals that laser absorptivity predominantly governs the overall thermal distribution, whereas shape parameters primarily influence the central melt pool temperature. Accordingly, a sequential optimization of absorptivity and shape parameters was implemented. Collectively, this two-step approach reduced the average deviation between measured and simulated temperatures from 18.7% to 9.63%, and diminished molten pool geometry errors—width, length, and depth—from 42%, 48%, and 43% to 9.6%, 19%, and 6.6%, respectively. The results demonstrate that the synergistic optimization of material properties and heat source models substantially enhances the accuracy of temperature field simulations, offering a more reliable theoretical foundation for predicting clad layer performance in laser cladding processes.

Keywords: laser cladding; aluminum alloys; Fe313 alloy; temperature field simulation; dilution ratio; thermophysical properties calibration; heat source optimization

Check for updates

Academic Editor: Alessandro Latini

Received: 18 August 2026
Revised: 9 September 2026
Accepted: 16 September 2026
Published: 21 September 2026

Copyright: © 2026 by the authors. Licensee MDPI, Basel, Switzerland. This article is an open access article distributed under the terms and conditions of the Creative Commons Attribution (CC BY) license.

1. Introduction

Aluminum alloys are widely used in aerospace and automotive industries due to their low density and high specific stiffness and strength [1]. These applications require

high wear and corrosion resistance, which can be effectively enhanced by laser cladding. However, laser cladding on aluminum alloys remains challenging. The high thermal conductivity and low laser absorptivity of aluminum substrates, combined with the thermophysical property mismatch with the cladding powder, tend to induce residual stresses and cracks. Clad quality is governed by interacting parameters such as laser power, scanning speed, and powder feed rate [2–4]. making process optimization a key research focus [5].

Temperature field simulation based on finite element method is an effective tool for predicting melt pool evolution, understanding thermal behavior, and optimizing parameters, thus reducing experimental costs and development cycles [6]. High-fidelity temperature field simulation is of critical importance for the accurate prediction of residual stresses and microstructural evolution. Consequently, considerable research efforts have been devoted to developing reliable temperature field simulation methodologies to guide experimental investigations, Various Gaussian heat source models—ranging from quasi-Gaussian surface distributions to three-dimensional volumetric representations and their derived forms—have been extensively employed to simulate temperature fields in laser cladding processes [7]. In one representative study, the combined effects of laser energy attenuation and powder particle heating were comprehensively incorporated, and the cladding layer geometry was successfully predicted using the element birth-and-death technique [8]. Another investigation established a transient three-dimensional finite element model within the ABAQUS CAE 2020 framework, wherein the thermophysical properties of the powder layer were determined via the Gusarov formulation [9], enabling predictive simulation of the coating morphology [10]. Furthermore, linear extrapolation and interpolation methods have been adopted to define the high-temperature thermophysical parameters of the material, thereby facilitating temperature field analysis of the coating geometry during wide-beam laser cladding. Constraints were imposed on the heat source shape parameters to maintain continuity of the dual-ellipsoidal heat flux density distribution [11]. In a subsequent study, the parameters of a transient three-dimensional finite element model for laser cladding temperature fields were calibrated using multidimensional melt pool dimensions extracted from metallographic cross-sections as matching targets [12].

However, the aforementioned studies have focused predominantly on the formulation and optimization of heat source models, which, while improving simulation accuracy to a certain extent, overlook the dynamic evolution of thermophysical properties (e.g., thermal conductivity and specific heat capacity) induced by compositional gradients within the dilution zone—a factor that introduces non-negligible simulation deviations [13,14]. Moreover, the empirical determination of physical parameters for the clad zone materials inevitably introduces discernible variability into the simulation outcomes. Although surface treatment of aluminum alloys has been shown to enhance laser absorptivity [15], the experimental quantification of this parameter exhibits substantial variability, typically necessitating broad parameter selection ranges that propagate significant uncertainties into temperature field predictions.

To address these limitations, the present study employs Fe313 alloy powder deposited onto aluminum substrates as the model system. A transient three-dimensional temperature field finite element model was developed within the ABAQUS framework to systematically investigate the determination of cladding material thermophysical parameters and laser absorptivity, as well as their coupled effects on the simulation accuracy of molten pool temperature fields. The objective is to establish robust methodologies for enhancing predictive fidelity in laser cladding thermal modeling.

2. Experimental Procedure and Temperature Monitoring Scheme in Laser Cladding

Laser cladding experiments were conducted using a Model HLB-F2000 continuous-wave fiber laser (wavelength: 1064 nm, maximum power: 2 kW), with the experimental setup illustrated in Figure 1. The substrate material was ZL101 aluminum alloy plates (dimensions: 50 mm × 50 mm × 10 mm), whose chemical composition is listed in Table 1. An iron-based self-fluxing alloy powder, Fe313 (particle size: 88–120 μm, melting point: ≈1500 °C), was employed, with its detailed composition provided in Table 2. The pre-placed powder layer measured 40 mm × 2 mm with a thickness of 0.3 mm. Laser cladding was performed at a laser power P = 800 W, a scanning speed v = 8 mm/s, and a defocusing distance of S = 20 mm, which produced a laser spot diameter of 1.92 mm. The process was carried out under an argon shielding atmosphere without workpiece preheating, yielding clad layers with dilution rates of 10%–20%.

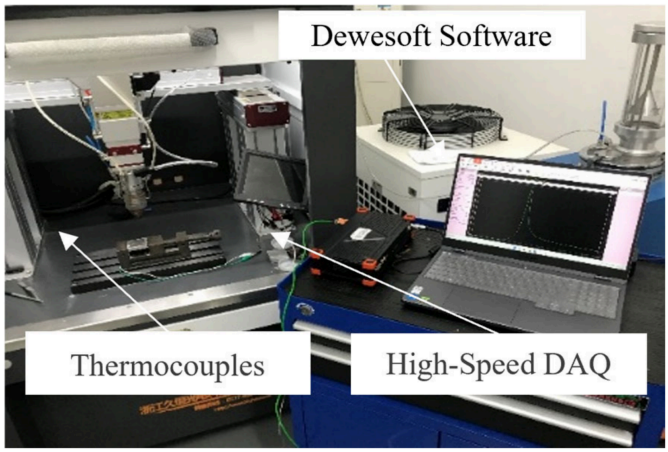

Figure 1. Schematic of the laser cladding experimental setup.

Table 1. ZL101 Chemical Composition (mass, wt.%).

Materials	Si	Mg	Fe	Cu	Zn	Ti	Al
ZL101	6.5~7.5	0.25~0.45	0.5	0.1	0.15	0.1	Bal.

Table 2. Chemical composition of the coating powder (mass, wt.%).

Powders	C	Si	B	Cr	Mn	Fe
Fe313	0.1~0.2	1.0~1.5	1.0~1.5	14–18	0.2~0.5	Bal.

A Cartesian coordinate system was defined with the origin "O" at the center of the substrate surface. The laser scanning direction, cladding width direction, and melt pool depth direction were designated as the *y*-, *x*-, and *z*-axes, respectively. Observation points R1–R10 were positioned along the negative *z*-axis (downward) and the positive *x*-axis (laterally outward) from the origin O, as illustrated in Figure 2.

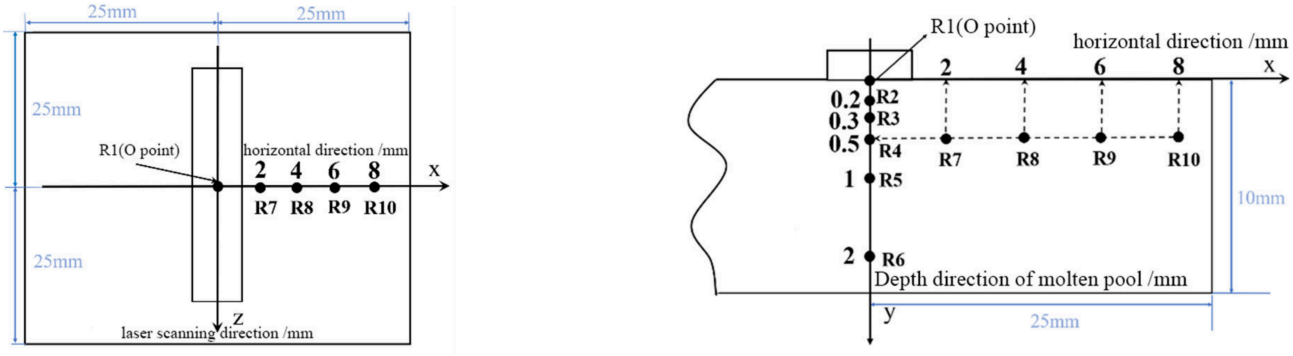

Figure 2. Layout of thermocouple monitoring positions: (**a**) Top View; (**b**) Cross-Sectional View.

Thermocouples were sequentially installed at each observation point. Specifically, a WRE3-WRE25 thermocouple with higher temperature measurement range was embedded at point R1, as it is located within the high-temperature molten pool during laser cladding. For the remaining observation points where temperatures remain below the melting point of aluminum alloy, K-type (NiCr-NiSi) thermocouples were employed. The thermocouple arrangement follows a non-uniform distribution pattern to accommodate thermal gradient variations. In high thermal gradient regions near the molten pool, observation points are densely spaced (R2-R5 at *z*-axis offsets of 0.2 mm, 0.3 mm, 0.5 mm, 1 mm, and 2 mm below substrate surface, respectively). In lower temperature regions with gradual thermal gradients, the spacing becomes progressively coarser (R7-R10 maintain constant 0.5 mm depth below surface with *x*-axis offsets of 2 mm, 4 mm, 8 mm, and 10 mm, respectively), as detailed in Figure 2b. The thin-foil thermocouples were embedded in a "sandwich" configuration and connected to a high-speed data acquisition system for temperature output, with the integrated Dewesoft software X3 (64-bit) employed for temperature data analysis.

3. Optimization of Thermophysical Parameters in Laser Cladding Molten Pool

3.1. Development of the Heat Source Model for Laser Cladding Simulations

A three-dimensional finite element model was developed in ABAQUS to simulate the temperature field during laser cladding, incorporating a user-defined DFLUX subroutine to implement a moving double-ellipsoidal heat source. The geometric dimensions of the substrate and coating models were determined based on actual workpiece measurements. The ZL101 aluminum alloy substrate was modeled with dimensions of 50 mm × 50 mm × 10 mm, and the Fe313 coating was modeled with dimensions of 40 mm × 2 mm × 0.3 mm. Given that the melt pool center exhibits elevated temperatures and steep thermal gradients, a refined mesh was adopted in the heat source traversal region to accurately capture the temperature distribution in the vicinity of the melt pool. A gradual transition to coarser elements with increasing edge length was employed in the regions remote from the heat source path. The entire model comprised a total of 145,070 elements, as illustrated in Figure 3.

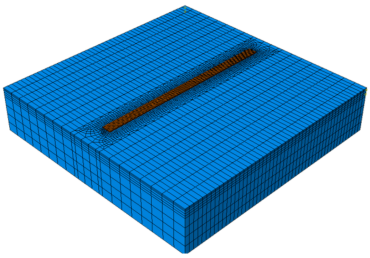

Figure 3. Geometric model and mesh configuration for single-track laser cladding.

The simulation is based on the following key assumptions: (1) both the aluminum alloy substrate and the coating material are treated as continuous and isotropic media; (2) the molten pool, formed by the mixture of the workpiece and coating materials, is compositionally [16] homogeneous and isotropic; (3) forced convection, driven by the coaxial shielding gas and the airflow from the air-purification system, dominates heat transfer; (5) the moving double-ellipsoidal heat source represents the laser irradiation on the pre-placed powder, thereby forming the molten pool; and (8) mass loss due to high-temperature vaporization is neglected [17].

$$\left.\begin{aligned} q(x,y,z,t) &= \frac{6\sqrt{3}f_f q\eta}{a_f bc\pi\sqrt{\pi}} exp\left(-\frac{3(x-vt)^2}{a_f^2}-\frac{3y^2}{b^2}-\frac{3z^2}{c^2}\right) \rightarrow (A) \\ q(x,y,z,t) &= \frac{6\sqrt{3}f_r q\eta}{a_r bc\pi\sqrt{\pi}} exp\left(-\frac{3(x-vt)^2}{a_r^2}-\frac{3y^2}{b^2}-\frac{3z^2}{c^2}\right) \rightarrow (B) \end{aligned}\right\} \quad (1)$$

The heat source model is defined by Equation (1), where q represents the laser power, η denotes the laser's thermal efficiency, and v indicates the scanning speed of the heat source relative to the workpiece. The shape parameters of the heat source model (a_f, a_r, b, c) are determined based on the actual dimensions of the molten pool, as illustrated in Figure 4. To ensure continuity of the heat flux density at the boundary between the front and rear ellipsoids, the shape parameters are constrained by Equation (2), which enforces the following condition:

$$\frac{f_f}{a_f} = \frac{f_r}{a_r} \quad (2)$$

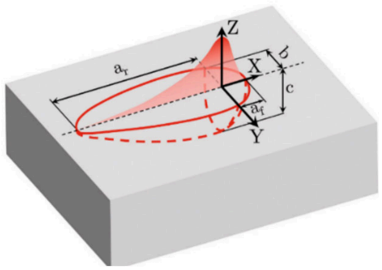

Figure 4. Double-ellipsoidal heat source models.

The laser absorptivity of the material is estimated using the Hagen–Rubens equation [18]:

$$A = \sqrt{8\varepsilon_0\omega\rho} = 354.67\sqrt{\rho} \quad (3)$$

where $\omega = 2\pi c/\lambda$, is the angular frequency (with λ = 1064 nm for the fiber laser). ε_0 is the vacuum permittivity, and ρ is the electrical resistivity.

Since the laser beam undergoes multiple reflections on the surfaces of metal powder particles before being absorbed, the powder morphology significantly affects the effective

absorptivity. To account for this geometric effect, the modified absorptivity A_p is calculated using Gusarov's model [19]. The intermediate variables are defined as:

$$\alpha = \sqrt{1 - \frac{2}{3}\omega - \frac{1}{3}\omega^2}, \omega = 1 - A \tag{4}$$

And the effective absorptivity is then given by:

$$A_p = \frac{3}{4} \cdot \frac{1 - \omega + 3a}{1 + 2a} \tag{5}$$

For the present parameters, this yields A_p = 0.75.

The workpiece surface away from the molten pool is subject to forced convection, with a convective heat transfer coefficient of 50 W/(m^2·K). In the molten pool region, the total heat transfer coefficient of the molten metal is determined following Vinokurov [20] as:

$$h_v^* = 2.41 \times 10^{-3} \varepsilon T^{1.61} \tag{6}$$

where the emissivity of the workpiece is set to 0.2. To account for the convection effects inside the pool, Yan et al. [21] proposed a method incorporating the influence of thermocapillary forces, i.e., Marangoni convection, on fluid motion to compute the melt boundary [22]. Accordingly, the thermal conductivity is modified [23] as:

$$\lambda^* = a\lambda \text{ for} T > T_m \tag{7}$$

3.2. Composition and Thermophysical Properties of the Mixed Dilution Zone

Figure 5 shows a cross-section of the clad coating, where s_1 and s_2 denote the areas of the Fe313 deposition zone and the dilution zone (mixture of substrate and coating), respectively [24]. The dilution rate D is then given by Equation (8) [25]:

$$D = \frac{S_2}{S_1 + S_2} \tag{8}$$

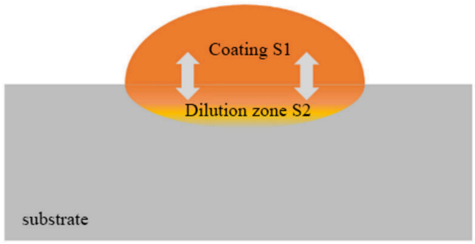

Figure 5. Coating Cross-Section Schematic.

With the dilution control target specified as $D = 10\%$, the elemental composition ratios in the mixed material of the dilution zone were calculated using Equation (9). Based on these results, the temperature-dependent thermophysical properties of the mixed material in the dilution zone were then obtained via JMatPro software (jmatPro_7.0) simulations, as presented in Figure 6.

$$w(B) = \frac{\rho_{Fe313} \times S_1}{\rho_{ZL101} \times S_2 + \rho_{Fe313} \times S_1} \times w_{Fe313}(B) + \frac{\rho_{ZL101} \times S_2}{\rho_{ZL101} \times S_2 + \rho_{Fe313} \times S_1} \times w_{ZL101}(B) \tag{9}$$

where ρ_{Fe313} represents the density of Fe313 alloy, ρ_{ZL101} denotes the density of ZL101 alloy, $w_{Fe313}(B)$ indicates the mass fraction of B in Fe313 material; $w_{ZL101}(B)$ refers to the mass fraction of B in ZL101 material.

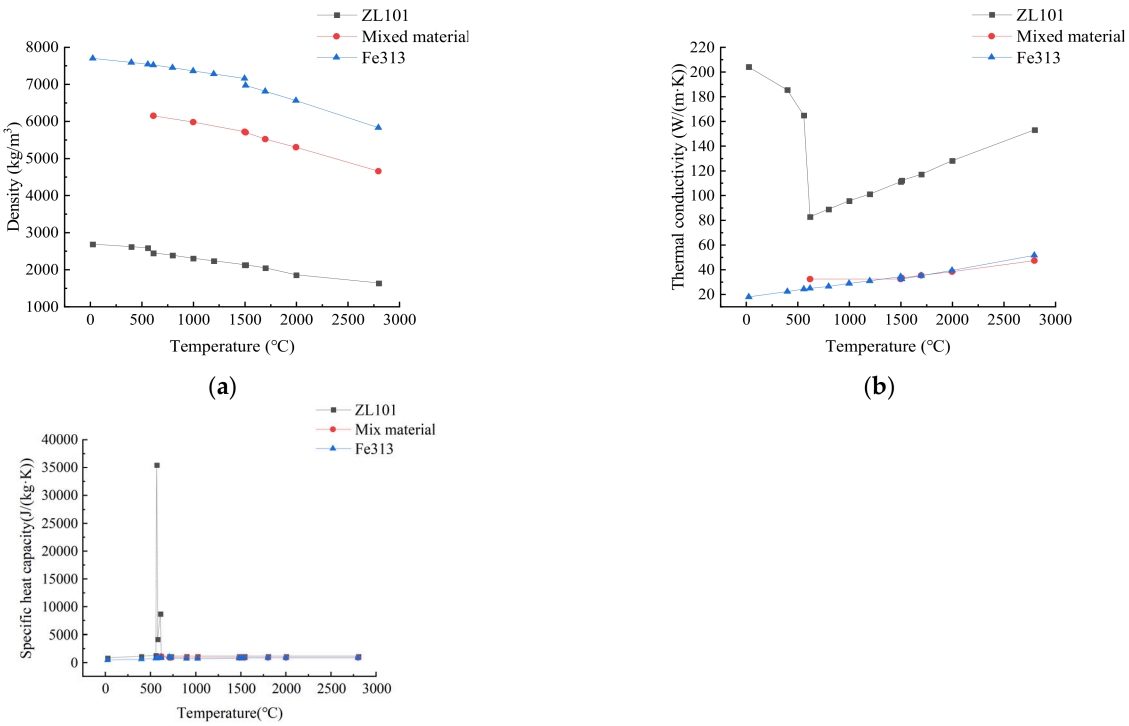

Figure 6. Thermo-physical Properties of Materials: (**a**) Densities of ZL101, Fe313 and mixed materials; (**b**) Thermal Conductivity of ZL101, Fe313 and Mixed Materials; (**c**) Specific heat capacity of ZL101, Fe313 and Mixed Materials.

The composite exhibits an intermediate density relative to the substrate and cladding materials. Its thermal conductivity, however, remains below that of both constituents yet shows a positive correlation with temperature. Accordingly, over the melting-to-peak temperature range, both density and thermal conductivity in the dilution zone must be treated as temperature-variant, whereas the specific heat, given its negligible temperature sensitivity, can be assumed constant.

3.3. Effect of Dilution Zone Material Parameters on Thermal Simulation Accuracy

For comparison with the experimental measurements, the upper and lower regions were assigned the original parameters of the powder and substrate, respectively, with the workpiece surface as the boundary. An improved method using modified mixed-material parameters for the molten zone is also evaluated against the same experimental data. Figure 7 compares the simulated temperatures at the observation points obtained by both methods with the measured values. The results show that: (1) both methods underestimate the molten pool temperature relative to the experiments, with the original-parameter method producing larger deviations, particularly near the pool; (2) the modified-parameter method significantly improves the high-temperature prediction, reducing the deviation at the pool center from 41% to 17% and the average deviation across all points from 18.7% to 16.7%. Thus, proper modification of dilution-zone material parameters, as validated by the experimental comparison, can effectively improve the thermal simulation accuracy in the molten pool region.

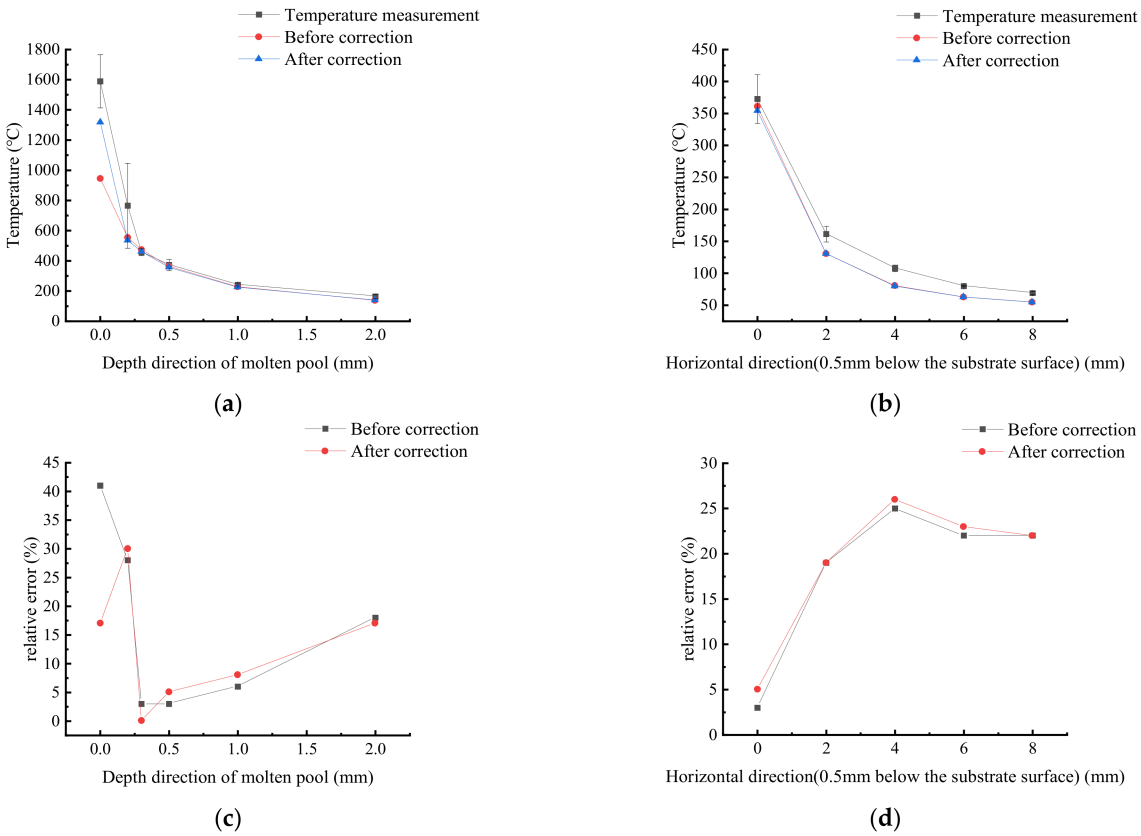

Figure 7. Temperature comparison and deviations at observation points: (**a**) peak temp. at R1–R6; (**b**) peak temp. at R4, R7–R10; (**c**) Relative deviations: R1–R6; (**d**) Relative deviations: R4, R7–R10.

4. Impact of Heat Source Model Parameters on Cladding Temperature Field Simulation

4.1. Key Heat Source Parameters from Sensitivity Analysis

The simulation results of the cladding temperature field are governed by not only material properties but also heat source shape parameters. In practice, these shape parameters are typically selected and optimized within empirical ranges drawing on relevant literature in order to minimize deviations between simulated and measured temperatures. To systematically identify the key parameters that require correction and to determine their optimization priority, this study performs a sensitivity analysis that calculates the sensitivity coefficients of peak temperatures at the observation points with respect to each parameter. These coefficients quantitatively evaluate the influence of each parameter on the simulation results, enabling the identification of the most influential parameters. The optimization strategy then prioritizes the correction of high-sensitivity parameters, with secondary parameters adjusted gradually thereafter [26].

The sensitivity coefficient S is calculated by Equation (10):

$$S(x) = \frac{\left|\frac{\Delta F}{F}\right|}{\frac{\Delta x}{x}} \tag{10}$$

Here, x represents the preset baseline value assigned to a given model's parameter. In the simulation, the thermal cycle at each observation point reaches a peak temperature F. A perturbation of Δx is applied to the parameter. And the corresponding change in the peak temperature is recorded as ΔF he sensitivity coefficient S is then calculated as the relative change in temperature per unit relative change in the parameter. Figure 8 presents the

peak-temperature increments at the monitored points when each parameter is increased by 10% from its baseline value. The results indicate that η, a_f, b and c exert a noticeable influence on the observed temperatures, whereas h, α and ε have a weaker effect.

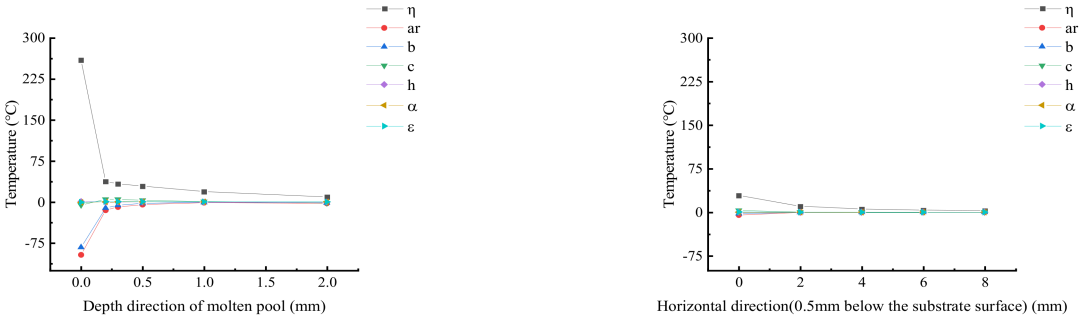

Figure 8. Peak temperature increments at observation points due to 10% parameter increases: (**a**) Temperature peaks: R1–R6; (**b**) Temperature peaks: R4, R7–R1.

Accordingly, the primary parameters affecting the temperature predictions, ranked in descending order of influence, are: laser absorptivity (η), followed by the heat source shape coefficients a_f, b, and c.

4.2. Calibration of Laser Absorptivity Parameters and Resulting Effects in Thermal Simulation

Laser absorptivity (η) and heat source geometry parameters (a_f, b, and c) significantly influence temperature field predictions; however, these parameters remain mutually unconstrained. To address this, we employ a pattern search optimization algorithm for simultaneous calibration, iteratively combining exploratory searches and pattern moves to minimize the discrepancies between simulated and experimental temperatures at the observation points [27].

Specifically, the laser absorptivity was optimized with an initial value of $X_1 = 0.75$, a search range of [0.75,1], an initial step size of 0.075, a step contraction factor of 0.5, and a termination threshold of 0.025. The optimization converged to a final absorptivity of 0.99. Figure 9 compares the measured and simulated temperatures before and after absorptivity calibration, including both depth-wise temperature profiles at the molten pool center and the transverse temperature distributions 0.5 mm below the substrate surface. Moreover, as shown in Table 3, the temperature deviations at all observation points were significantly reduced after calibration, demonstrating the effectiveness of the proposed method.

Table 3. Mean relative deviation between simulated and measured temperatures.

	e_1 (%)	e_2 (%)	Mean Δ%
Original	9.4	22.5	16.7
Revised	18	7.3	15.3

The calibrated increase in laser absorptivity enhances energy input and thereby expands the molten pool. As shown in Figure 10a,c, the simulated temperatures at the depth-wise observation points rise markedly, with error e_1 increasing from 9.4% to 18%.

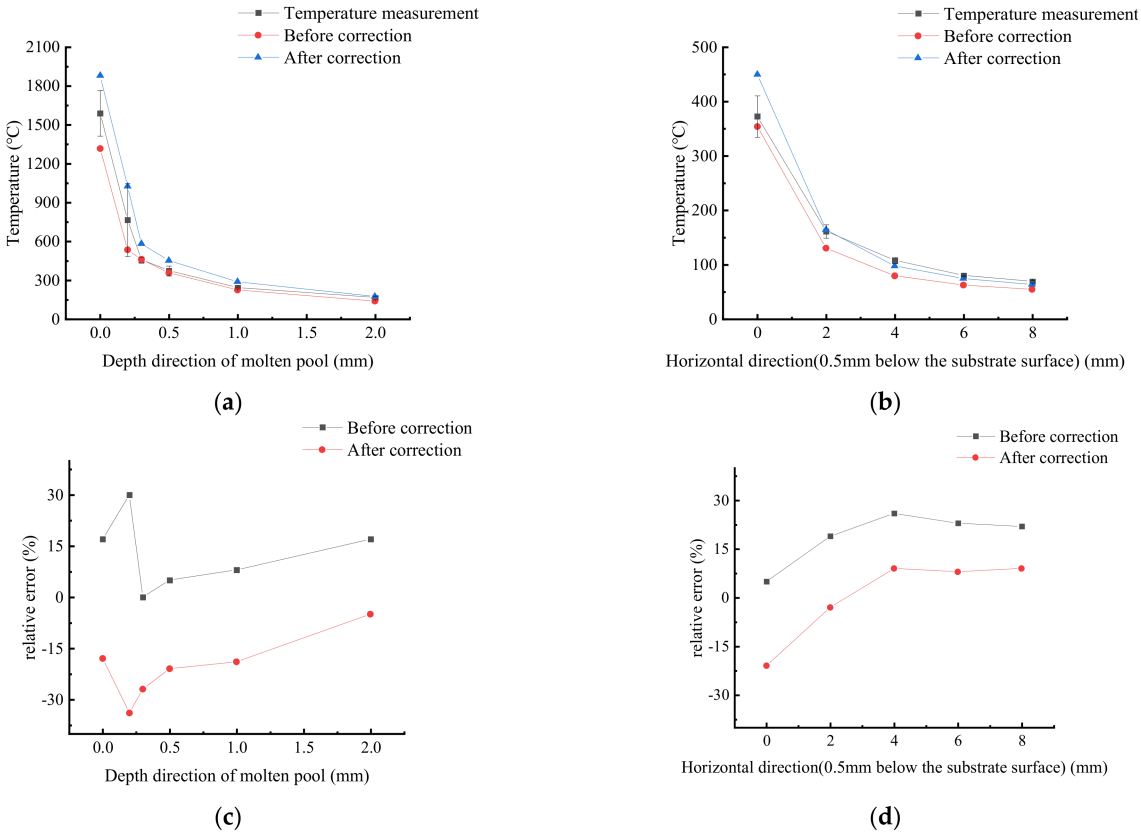

Figure 9. Temperature profiles before and after laser absorptivity correction: (**a**) Temperature distribution: R1–R6; (**b**) Temperature distribution: R4, R7–R10; (**c**) Temperature deviations: R1–R6; (**d**) Temperature deviations: R4, R7–R10.

The most pronounced variation occurred at point R2, where the relative error shifted from 30% to −34%. This indicates that the enlarged molten pool shifts the original boundary point R2 into a zone characterized by a steep temperature gradient. Additionally, minor displacements in thermocouples placement may have contributed to considerable measurement fluctuations and errors at this specific location. Overall, these experimental findings highlight key factors underlying simulation-measurement discrepancies near molten pool boundaries, specifically the morphological evolution of the pool and the precision of thermocouple positioning.

The increased energy input yielded a dual effect. On one hand, the expanded molten pool caused overestimated simulated temperatures along the depth direction, as evidenced by a −34% error at point R2. On the other hand, simulation accuracy improved for the distal horizontal observation points (R7–R10), where the average deviation e_2 decreased from 15.2% to 13.2%.

Overall, the average deviation across all monitoring points after calibration dropped from 16.7% to 15.3%. Nevertheless, temperature overestimation persists in the central region of the molten pool, indicating localized energy oversaturation within the current model. This highlights the necessity of further optimizing the heat source shape parameters to achieve finer spatial control over the thermal distribution.

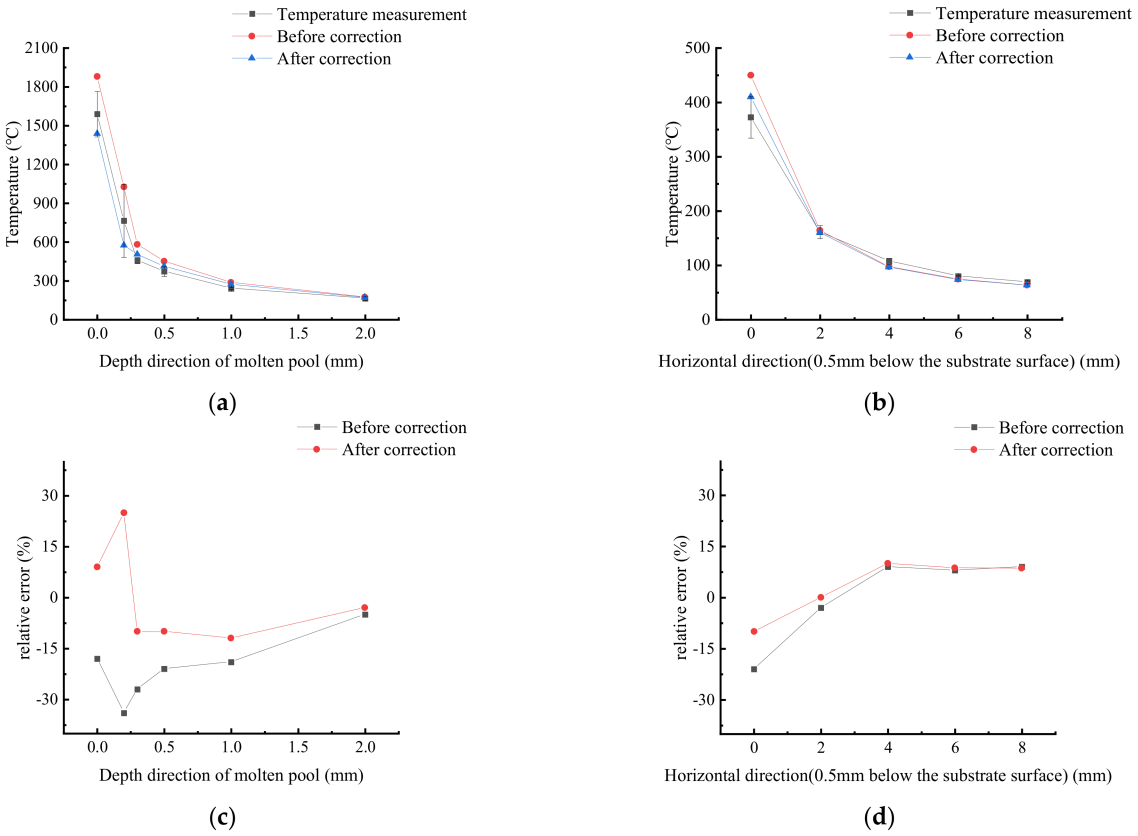

Figure 10. Comparison of simulated temperatures (before and after calibration) with measured data: (**a**) Near-field (R1–R6) temperature; (**b**) Far-field (R7–R10, referencing R4) temperature; (**c**) Near-field relative deviations; (**d**) Far-field relative deviations.

4.3. Calibration of Heat Source Shape Parameters for Thermal Simulation Accuracy

The heat source shape parameters were similarly calibrated using the pattern search method. Parameter a_f and $a_r/2$ and was initialized at $X_2 = 0.75 \times 10^{-3}$m, with a search range of $[0.75 \times 10^{-3}, 0.1 \times 10^{-3}$ m]. Parameter c was initialized at $X_3 = 0.5 \times 10^{-3}$m, with a search range $\left[0 - 0.7 \times 10^{-3}\text{m}\right]$. For both parameters, the initial step size was set to 0.1×10^{-3}m, the step contraction factor to 0.5×10^{-3}, and termination threshold of 0.05×10^{-3}. The optimization converged to final values of $a_f = 1.0 \times 10^{-3}$m, and $c = 0.2 \times 10^{-3}$m, as detailed in Table 4.

Table 4. Heat source shape parameters before and after calibration.

	$a_f/10^3 \cdot$m	$a_r/10^3 \cdot$m	b/$10^3 \cdot$m	c/$10^3 \cdot$m
Previous	0.75	1.5	0.75	0.5
Update	1.0	2.0	1.0	0.2

Figure 10 presents the simulation results obtained using the calibrated heat source parameters. The adjusted parameters redefined the energy distribution, substantially reducing the depthwise extent of the heat-affected zone. At observation points R1–R6 (excluding R2), the average error e_1 dropped markedly from 18% to 8.8%. Meanwhile, the error at point R2 shifted from −34% to 25%, indicating its new position outside the modified molten pool boundary. For the distal points R7–R10, the average error e_2 improved only slightly, from 7.3% to 6.8%, and the peak temperatures in the thermal cycles remained nearly unchanged. This demonstrates that the modified heat source geometry primarily influences far-field temperatures primarily via thermal conduction, with a negligible direct

effect. The optimal parameter combinations and corresponding errors (Tables 4 and 5) confirm that parameter optimization effectively enhanced simulation accuracy in the molten pool region.

Table 5. Average relative temperature deviations at orthogonal observation points.

	e_1	e_2	Mean Δ%
Previous	18%	7.3%	15.3%
Update	8.8%	6.8%	9.63%

5. Melt Pool–Guided Laser Cladding Simulation Calibration

During in situ monitoring, a high-speed camera (5KF20; 1920 × 1080 resolution; 1 µs exposure) was used to dynamically capture the surface profile of the clad track. The planar dimensions of the melt pool, derived from calibration, are documented in Figure 11. Complementary microscopic examination of polished cross-sectional clad samples quantified the melt pool depth and width, as presented in Figure 12.

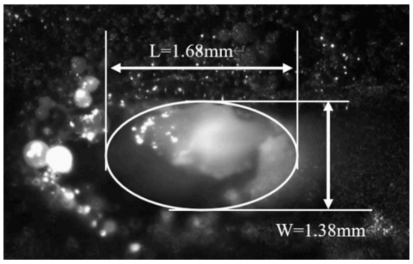

Figure 11. Overhead view of melt pool imaging.

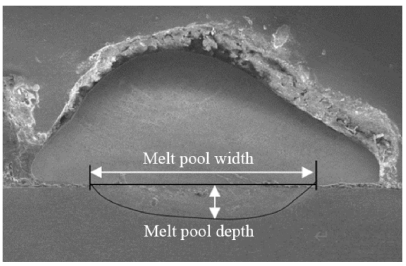

Figure 12. Cross-Sectional View of Coating.

Figure 13 presents the numerically simulated temperature field for laser cladding process. The melt pool boundaries were identified using the alloy liquidus isotherm, from which the corresponding dimensions were extracted. A comparative analysis of the measured and simulated melt pool dimensions (length, width, and depth) is summarized in Table 6. After calibration, the results show substantial reductions in deviation: depth deviation decreased from 21% to 0.5%, width deviation from 42% to 9.6%, and length accuracy improved by 28.4 percentage points These improvements demonstrate that the refined model possesses an enhanced capability to characterize melt pool morphology with significantly greater, thereby validating the effectiveness of the optimization methodology precision.

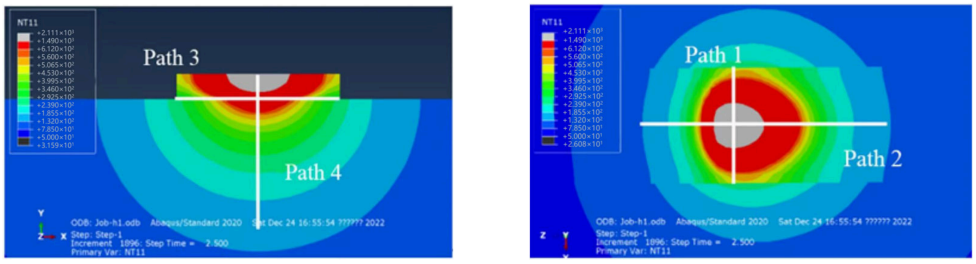

(**a**) (**b**)

Figure 13. Simulated temperature fields and melt pool geometry: (**a**) Vertical cross-section of melt pool; (**b**) Plan view of melt pool.

Table 6. Comparison of measured and simulated melt pool dimensions.

Melt Pool Dimensions	W/mm	L/mm	W/L	w/mm	h/mm	w/h
Measured values	1.38	1.68	0.82	1.35	0.19	7.1
Adjusted simulated values	1.27	1.35	0.94	1.26	0.19	6.6
Pre-adjustment deviation	42%	48%	-	43%	21%	-
Post-adjustment deviation	9.6%	19.6%	-	6.6%	0.5%	-

6. Conclusions

This study established a three-dimensional transient thermal field simulation model for laser cladding of Fe313 alloy on aluminum substrates using the Finite Element Method. To minimize discrepancies between in situ temperature measurements and simulated outputs, we systematically refined critical thermophysical parameters through a synergy of dilution-ratio calibration, absorptivity optimization, and heat-source morphology adjustment. The principal findings are summarized as follows:

1. Dilution-ratio-driven recalibration—based on the composition-dependent alloy mixing ratio within the fusion zone—reduced the mean relative temperature deviation at monitoring points from 18.7% to 16.7%, while simulation errors near the melt pool decreased by 24%. This confirms that accounting for dilution effects substantially improves the model's capability to resolve transient thermal distributions with industrial-grade fidelity.
2. Laser absorptivity optimization was performed via thermal field analysis. Using the Hagen–Rubens relation for the Fe313 alloy at 1064 nm and incorporating powder geometric effects through the Gusarov model, we determined a powder-state absorptivity range of 0.69–0.826. Comparative evaluation between simulated thermal profiles and experimental data identified optimal convergence at an absorptivity of 0.99. Despite residual uncertainty, this refined estimate provides critical insight into how laser absorption dynamics govern thermal field evolution.
3. Heat-source parameter optimization followed a stepwise strategy. Initial dual-ellipsoid source parameters were estimated from clad track width and melt pool depth. Subsequent sensitivity analysis of parameter effects on peak temperature, combined with a stepwise accelerated search algorithm, yielded optimized parameters that reduced the mean relative error at monitoring points from 16.7% to 9.63%, validating the effectiveness of this stepwise approach.
4. Guided by the dilution ratio as a target range, the synergistic optimization of molten-pool material properties, substrate laser absorptivity, and heat source morphology

produced a substantial cumulative enhancement in model accuracy: the deposited track surface width deviation decreased from 42% to 9.6%, track length deviation from 48% to 19%, melt pool width deviation from 43% to 6.6%, and melt pool depth deviation from 21% to 0.5%.

Collectively, the proposed synergy-driven parameter optimization framework offers a novel and effective technical pathway for enhancing the accuracy of laser cladding temperature field simulations and provides critical guidance for predictive thermal modeling in laser additive manufacturing processes.

Author Contributions: Conceptualization, F.Y.; methodology, B.Z. and F.Y.; software, B.Z.; validation, B.Z.; formal analysis, B.Z. and H.P.; investigation, B.Z. and H.P. and Y.C.; resources, F.Y. and X.W.; data curation, B.Z., H.P., Y.C. and H.-M.H.; writing—original draft preparation, B.Z. and F.Y.; writing—review and editing, F.Y., H.P., X.W. and Y.C.; visualization, H.P., Y.C. and H.-M.H.; supervision, F.Y.; project administration, F.Y.; funding acquisition, F.Y. All authors have read and agreed to the published version of the manuscript.

Funding: This research was supported by: Teaching Reform Research Project of Huaqiao University (HQJGYB2520); Natural Science Foundation of Xiamen City. (3502Z20227195).

Institutional Review Board Statement: Not applicable.

Informed Consent Statement: Not applicable.

Data Availability Statement: The raw data supporting the conclusions of this article will be made available by the authors on request.

Conflicts of Interest: The authors declare no competing interests.

References

1. Arriaga-Benitez, R.I.; Pekguleryuz, M. Recent progress in creep-resistant aluminum alloys for diesel engine applications: A review. *Materials* **2024**, *17*, 3076. [CrossRef]
2. Zhang, H.; Cheng, W.; Yin, Y.; Sun, Y.; Li, X. Microstructure and strengthening mechanism of a 316 stainless steel coating prepared by high-speed laser cladding on an aluminum alloy plate. *Arch. Civ. Mech. Eng.* **2024**, *25*, 15. [CrossRef]
3. Sui, Q.; Hu, N.; Su, Y.; Wang, Y.; Song, X. Tensile property of 7075 aluminum alloy with strengthening layer by laser remelting cladding treatment. *Micromachines* **2023**, *14*, 2017. [CrossRef]
4. Zhang, P.; Li, Y.; Li, L.; Su, K.; Zhang, H.; Yu, L.; Zhao, Z. Microstructure and properties of Ti/TiBCN coating on 7075 aluminum alloy surface by Laser cladding. *China Surf. Eng.* **2018**, *31*, 159–164.
5. Wei, C.; Zhao, Z.; Du, W.; Bai, P. Numerical simulation and crack suppression study on high-speed laser cladding of ZL101 aluminum alloy. *JOM* **2024**, *76*, 4299–4313. [CrossRef]
6. Ye, W.-L.; Sun, A.-D.; Zhai, W.-Z.; Wang, G.-L.; Yan, C.-P. Finite element simulation analysis of flow heat transfer behavior and molten pool characteristics during 0Cr16Ni5Mo1 laser cladding. *J. Mater. Res. Technol.* **2024**, *30*, 2186–2199. [CrossRef]
7. Jiménez-Xamán, M.; Hernández-Hernández, M.; Tariq, R.; Landa-Damas, S.; Rodríguez-Vázquez, M.; Aranda-Arizmendi, A.; Cruz-Alcantar, P. Numerical simulations and mathematical models in laser welding: A review based on physics and heat source models. *Front. Mech. Eng.* **2024**, *10*, 1325623. [CrossRef]
8. Hu, Z.; Li, C.; Tian, D.; Li, X.; Wang, J.; Xu, Z.; Sun, X. Numerical simulation analysis of temperature distribution of NbC-Reinforced Ti-Based composite coating by laser cladding. *Metals* **2023**, *13*, 1348. [CrossRef]
9. Liu, C. *Numerical Simulation of Temperature Field and Stress Field During Laser Cladding of Aluminium Alloy*; Shanghai University of Engineering Science: Shanghai, China, 2020.
10. Gao, J.; Wu, C.; Hao, Y.; Xu, X.; Guo, L. Numerical simulation and experimental investigation on three-dimensional modelling of single-track geometry and temperature evolution by laser cladding. *Opt. Laser Technol.* **2020**, *129*, 106287. [CrossRef]
11. Gery, D.; Long, H.; Maropoulos, P. Effects of welding speed, energy input and heat source distribution on temperature variations in butt joint welding. *J. Mater. Process. Technol.* **2005**, *167*, 393–401. [CrossRef]
12. Liu, H.; Li, M.; Qin, X.; Huang, S.; Hong, F. Numerical simulation and experimental analysis of wide-beam laser cladding. *Int. J. Adv. Manuf. Technol.* **2019**, *100*, 237–249. [CrossRef]
13. Li, J.; Li, X.; Zuo, D. Process test and temperature field simulation of the Al/Ti laser cladding coating above 7050 Aluminum alloy. *Laser Optoelectron. Prog.* **2014**, *51*, 173–180. [CrossRef]

14. Yao, M.; Kong, F.; Tong, W. A 3D finite element analysis of thermally induced residual stress distribution in stainless steel coatings on a mild steel by laser hot wire cladding. *Int. J. Adv. Manuf. Technol.* **2023**, *126*, 759–776. [CrossRef]
15. Hou, H.; Xie, Y.; Zhao, J. Experimental research on absorptivity of aluminum alloy cut by laser. *Surf. Technol.* **2016**, *45*, 193–198.
16. Xu, P.; Chen, L.; Yu, T. Simulation and experimental study on temperature field and flow field of laser cladding high-temperature Ni-based alloys. *Mater. Res. Express* **2024**, *11*, 126503. [CrossRef]
17. Goldak, J.; Chakravarti, A.; Bibby, M. A new finite element model for welding heat sources. *Metall. Trans. B* **1984**, *15*, 299–305. [CrossRef]
18. Deus, A.M.; Vilar, R. One-dimensional thermal model including the dependence of absorptivity on temperature using Hagen–Rubens equation. In *Laser Processing: Surface Treatment and Film Deposition*; NATO ASI Series; Mazumder, J., Conde, O., Villar, R., Steen, W., Eds.; Springer: Dordrecht, The Netherlands, 1996; Volume 307, pp. 195–201.
19. Gusarov, A.V.; Kruth, J.-P. Modelling of radiation transfer in metallic powders at laser treatment. *Int. J. Heat Mass Transf.* **2005**, *48*, 3423–3434. [CrossRef]
20. Vinokurov, V.A. *Welding Stresses and Distortion*; Baker, J.E., Translator; The British Library, Lending Division: Wetherby, UK, 1977; pp. 118–119.
21. Yang, L.; Peng, X.; Wang, B. Numerical modeling and experimental investigation on the characteristics of molten pool during laser processing. *Int. J. Heat Mass Transf.* **2001**, *44*, 4465–4473. [CrossRef]
22. Murugesan, A.; Biswas, K. Two-dimensional longitudinal modelling of SS410-Al_2O_3-SiC functionally graded composite heat transfer, fluid flow and molten pool dynamics during laser cladding. *J. Alloys Compd. Commun.* **2026**, *10*, 100164. [CrossRef]
23. Zhang, Z.; Kovacevic, R. A thermo-mechanical model for simulating the temperature and stress distribution during laser cladding process. *Int. J. Adv. Manuf. Technol.* **2019**, *102*, 457–472. [CrossRef]
24. Jiang, Y.; Cheng, Y.; Zhang, X.; Yang, J.; Yang, X.; Cheng, Z. Simulation and experimental investigations on the effect of Marangoni convection on thermal field during laser cladding process. *Optik* **2020**, *203*, 164044. [CrossRef]
25. Tian, H.; Chen, X.; Yan, Z.; Zhi, X.; Yang, Q.; Yuan, Z. Finite-element simulation of melt pool geometry and dilution ratio during laser cladding. *Appl. Phys. A* **2019**, *125*, 485. [CrossRef]
26. Li, P.; Lu, H. Sensitivity analysis and prediction of double ellipsoid heat source parameters. *Trans. China Weld. Inst.* **2011**, *31*, 89–91. (In Chinese)
27. He, L.; Bai, R.; Lei, Z.; Liu, D.; Jiang, H.; Xu, Y.; Zhu, J. Parametric Study of Inverse Heat Source Model Based on Molten Pool Morphology for Selective Laser Melting. *Coatings* **2025**, *15*, 497. [CrossRef]

Disclaimer/Publisher's Note: The statements, opinions and data contained in all publications are solely those of the individual author(s) and contributor(s) and not of MDPI and/or the editor(s). MDPI and/or the editor(s) disclaim responsibility for any injury to people or property resulting from any ideas, methods, instructions or products referred to in the content.